DOI: 10.1021/ma902631e

Macromolecules
ARTICLE

Hierarchical Self-Assembly and Dynamics of a Miktoarm Star *chimera* Composed of Poly(γ-benzyl-L-glutamate), Polystyrene, and Polyisoprene

A. Gitsas and G. Floudas*

Department of Physics, University of Ioannina, P.O. Box 1186, GR-45110 Ioannina, Greece, and Foundation for Research and Technology-Hellas, Biomedical Research Institute (FORTH-BRI), P.O. Box 1385, GR-71110, Heraklion, Crete, Greece

M. Mondeshki, I. Lieberwirth, and H. W. Spiess

Max-Planck-Institut für Polymerforschung, D-55021 Mainz, Germany

H. Iatrou and N. Hadjichristidis

Department of Chemistry, University of Athens, Panepistimiopolis, Zografou, GR-15771 Athens, Greece

A. Hirao

Polymeric and Organic Materials Department, Graduate School of Science and Engineering, Tokyo Institute of Technology, Tokyo, 152-8552, Japan

Received November 28, 2009; Revised Manuscript Received January 13, 2010

ABSTRACT: The hierarchical self-assembly at the submicrometer, nanometer and α-helical length scales has been studied in a miktoarm star rod−coil *chimera* composed of poly(γ-benzyl-L-glutamate) (PBLG), polystyrene, and polyisoprene blocks by X-ray scattering, solid state NMR, and transmission electron microscopy. The propensity of the rod block toward α-helices that are further hexagonally packed gives rise to pure PBLG domains and induces the partial mixing of the two amorphous blocks. These structural results were confirmed by independent dynamic probes at the segmental and α-helical level by NMR and dielectric spectroscopy, respectively.

I. Introduction

The phase state of coil−coil block copolymers has been investigated in detail over the past two decades.[1−3] It is known, for example, that apart from the strength of molecular interactions (i.e., the Flory−Huggins interaction parameter χ), the degree of polymerization N, and the composition, other parameters, such as, fluctuations, molecular architecture, and conformational asymmetry, play a major role in determining the phase state. The extreme case of conformational asymmetry in rod−coil copolymers, on the other hand, is much less investigated. In the latter case, the rigidity of the stiff block can result either from the intramolecular hydrogen bonds that stabilize α-helices in polypeptides[4] or by the delocalization of π-electron clouds in π-conjugated polymers.[5] The former rod−coil copolymers, in particular, combine the ability of polypeptides to form a reversible hydrogen bonded network of α-helical (or β-strand) secondary structures within the rod-like polypeptide block with the statistical nature of synthetic random-coil polymers[6,7] Moreover, the ability of the rigid block to form liquid crystals significantly alters the phase behavior. The Hamiltonian, apart from the usual Flory−Huggins repulsion between the rod and coil blocks now contains a second term that describes the excluded volume interaction between the rod blocks favoring their alignment given by the Maier−Saupe interaction. Thus, nanophase separation is driven by the Flory−Huggins interactions, whereas the orientational ordering is driven by the Maier−Saupe interactions favoring a smectic C phase in the rod-rich region.[8]

In the presence of strong Maier−Saupe interactions, the phase diagram is very asymmetric in comparison to the coil−coil diblock case. The critical point is shifted to the rod-rich part and the phase diagram is now dominated by the lamellar phase.[8] There are several examples from different rod−coil polypeptide/amorphous polymer hybrids that exhibit this phase state asymmetry. For example, a linear poly(γ-benzyl-L-glutamate)-*b*-poly(dimethyl siloxane)-*b*-poly(γ-benzyl-L-glutamate) (PBLG-*b*-PDMS-*b*-PBLG) triblock copolymer[9] with a rod volume fraction of $f_{PBLG} = 0.82$, forms a lamellar nanodomain. Similarly, in a PBLG-*b*-polyglycine diblock copolymer,[10] a lamellar nanodomain was obtained for $f_{PBLG} = 0.79$.

As with nonlinear coil−coil block copolymers,[11,12] it is anticipated that nonlinear (miktoarm, star) polypeptide/hybrid copolymer topologies would affect the nanodomain self-assembly and overall phase state. Ideally, one would like to know how the star topology affects the phase-boundary, the nanodomain spacing, and the type and persistence of peptide secondary structure. This issue is of particular interest as recent reports have demonstrated that the confinement[13,7] and packing efficiency[10,14,15] can affect the stability of the polypeptide secondary structure.

There have been only a few reports of the synthesis of complex multiblock polymer/polypeptide hybrid copolymers (called molecular *chimeras*). The first,[16] on polypeptide-based linear multiblock multicomponent hybrids, applied the organonickel method. Subsequently, two groups addressed the synthesis of molecular *chimeras* by a combination of atom transfer radical

*To whom correspondence should be addressed. E-mail: gfloudas@cc.uoi.gr.

 Published on Web 01/27/2010 © 2010 American Chemical Society

Scheme 1. Schematic of the Miktoarm Star Chimera (PS)(PI)(PBLG)

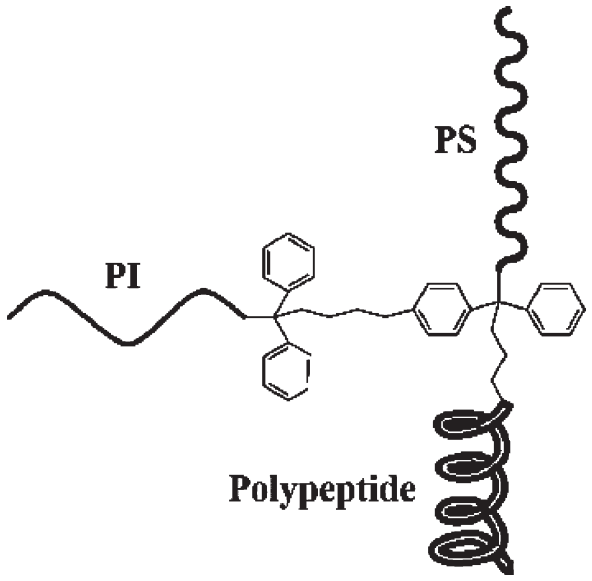

polymerization (ATRP) and ring-opening polymerization (ROP) to produce star block copolymers consisting of three polystyrene-*b*-poly(γ-benzyl-L-glutamate) (PS-*b*-PBLG) arms[17] as well as a polystyrene-*b*-poly(glutamic acid) diblock (PS-*b*-PGA) and a 3-miktoarm PS-*b*-$(PGA)_2$ star copolymer.[18] More recently,[19] the synthesis of a series of novel multiblock multicomponent miktoarm star hybrid has been reported that is based on a combination of living anionic and ring-opening polymerizations. In particular, the miktoarm star, composed from polystyrene (PS), polyisoprene (PI), and PBLG blocks (i.e., molecular *chimera*) combines multiple antagonistic interactions (Scheme 1); unfavorable interactions between the amorphous blocks and between the polypeptide and the amorphous blocks, with the propensity of PBLG to form intramolecular hydrogen bonds that stabilize α-helical segments. Yet, the star topology forces the three blocks to the star center, and this induces segmental mixing that may lead to the destabilization of the peptide secondary structure. In the present study we employ the (PS)(PI)(PBLG) miktoarm star and investigate the self-assembly and dynamics at the relevant length- and time-scales with X-ray scattering, solid state NMR, and dielectric spectroscopy. We ask, in particular, to what extent the propensity of the rod block to form α-helices that are hexagonally packed gives rise to pure PBLG domains and whether or not it induces partial mixing of the two amorphous blocks.

II. Experimental Section

Synthesis. The synthesis of the 3-miktoarm star *chimera* has been reported earlier in ref[19]. Briefly, the synthesis involved a combination of living anionic and ring-opening (ROP) polymerizations, using high vacuum techniques. With anionic polymerization, a diblock copolymer of PS and PI, bearing an amino functionality at the junction point, was synthesized by (a) reaction of PILi with 1-[4-(4-bromobutyl)phenyl]-1-phenylethylene (DC4Br), (b) addition of PSLi to the remaining double bond of the DC4 moiety, (c) reaction of the active Li species with 1-(3-bromopropyl)-2,2,5,5-tetramethyl-aza-2,5-disilacyclopentane, and (d) deprotection of the amino group. The final miktoarm star was obtained by the ROP of γ-benzyl-L-glutamate *N*-carboxyanhydride, using the NH_2-in chain PS-*b*-PI as macroinitiator. The molecular characteristics are given in Table 1.

Differential Scanning Calorimetry (DSC). A Mettler Toledo star differential scanning calorimeter was used for the thermal analysis. The miktoarm star hybrid was first heated at a rate of 10 K/min to 543 K and subsequently cooled to 123 K with 10 K/min. A second heating run, with the same rate (shown in Figure 1), was used to identify the glass temperatures, T_g, and the width of the transition, ΔT_g. Three step-like changes in the heat flow can be identified at −66.5, 18, and 77 °C, reflecting, respectively, the PI, PBLG, and modified PS glass temperatures. We mention here that earlier works established the PBLG glass temperature at 18 °C. The presence of three glass temperatures in the star alone cannot prove nanophase separation. Additional structural and dynamic studies are required to address this point (see below).

Transmission Electron Microscopy (TEM). Prior to the TEM measurement, the bulk sample was block-stained prior to final ultramicrotomy of 60 nm thin sections. For the block-staining, an appropriate block of approximately 50 × 50 μm^2 face was trimmed from the bulk sample. Subsequently, it was exposed to OsO_4 vapor for 24 h at room temperature followed by ultramicrotomy of the stained block to 60 nm sections. Inspection of the sample was performed with a Tecani F20 (FEI company) transmission electron microscopy operated at 200 kV acceleration voltage, and a representative image is shown in Figure 2. To clarify the compositional structure, additional image processing was applied to selected micrographs: From the gray scale histogram of the image, one can distinguish three more of less separated brightness levels. By setting two intensity thresholds, the image pixel values were separated into high, medium, and low brightness and finally displayed using a false color image. This type of analysis revealed dark cylinders (PI) surrounded by a PI/PS region and followed by a continuous (bright) PBLG phase.

Solid State NMR. The solid state NMR experiments were performed on a Bruker Avance spectrometer with a ^1H frequency of 500.1 MHz and ^{13}C frequency of 125.76 MHz. A Bruker double resonance probe, supporting rotors of 2.5 mm outer diameter at a spinning frequency of 20 kHz, was used in all cases. At high spinning frequencies, additional heating effects caused by bearing gas friction become significant. The sample temperatures have been corrected for these frictional heating effects following the procedure of ref 20. For all variable temperature (VT) solid state ^{13}C cross-polarization (CP) magic angle spinning (MAS) NMR experiments, an initial 90° pulse with 2.5 μs length and 2 s recycle delay were used. The duration of the variable amplitude contact pulse (80−100%)[21] was 1 ms and two-pulse phase-modulation (TPPM) ^1H decoupling scheme[22] was used while acquiring the ^{13}C signal. Two k transients were averaged for the experiments. Figure 3 provides the CPMAS NMR spectra of the PBLG and PS homopolymers together with the star, with the identification of the resonances.

X-ray Scattering. Both wide-angle and small-angle X-ray scattering (WAXS/SAXS) measurements have been performed from macroscopically oriented filaments[23] with a diameter of 0.5 mm using a pinhole collimator and a two-dimensional detector (Bruker) with 1024 × 1024 pixels. The extrusion temperature was 343 K. A graphite monochromator was used (λ = 0.154 nm), and the sample-to-detector distance was 7.25 cm. Measurements of 1 h long were made at several temperatures in the range 303−433 K in steps of 10 K on cooling and on subsequent cooling. The recorded 2D scattered intensities were integrated over the azimuthal angle and are presented as a function of the scattering wave vector q ($q = (4\pi/\lambda)\sin(2\theta/2)$, where 2θ is the scattering angle) in Figure 4. In the SAXS measurements, the sample-to-detector distance was set at 1.78 m. 2D images were obtained for different temperatures in the range $303 < T < 433$ K in 10 K intervals. However, the SAXS images showed increasing intensity at lower wave vectors and the absence of well-defined small-angle peaks.

Dielectric Spectroscopy (DS). The dielectric measurements were performed at different temperatures in the range 123−473 K, at atmospheric pressure, and for frequencies in the range from 10^{-2} to 10^6 Hz using a Novocontrol BDS system composed of a frequency response analyzer (Solartron Schlumberger FRA 1260) and a broadband dielectric converter. The sample cell

Table 1. Molecular Characteristics of the 3-Miktoarm star

	precursor		Final star			
sample	PS, $M_n \times 10^{-3}$[a] (g/mol)	PI, $M_n \times 10^{-3}$[a] (g/mol)	$M_n \times 10^{-3}$[b] (g/mol)	$M_n \times 10^{-3}$[c] (g/mol)	composition[d] % (w/w)	M_w/M_n[b]
(PS)(PI)(PBLG)	10.0	13.0	33.3	35.0	32.3−39.2−28.5	1.09

[a] By SEC in THF at 40 °C. [b] By SEC-TALLS in DMF (0.1 N LiBr) at 60 °C. [c] Stoichiometric molecular weight. [d] By ^{1}H NMR in $CDCl_3$.

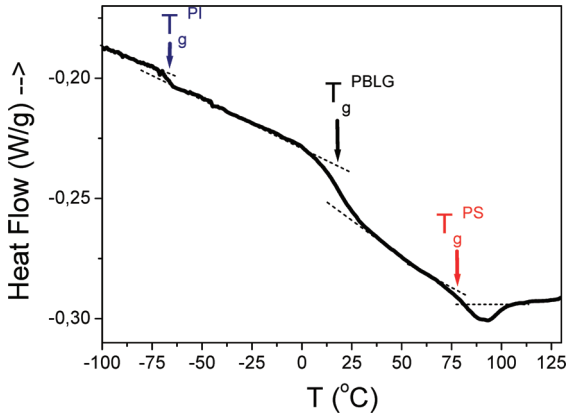

Figure 1. DSC thermogram of the miktoarm star obtained during the second heating run (rate 10 K/min). Three glass temperatures are shown by arrows that correspond to PI ($T_g^{PI} = -66.5$ °C), PBLG ($T_g^{PBLG} =$ 18 °C), and PS ($T_g^{PS} \sim 77$ °C).

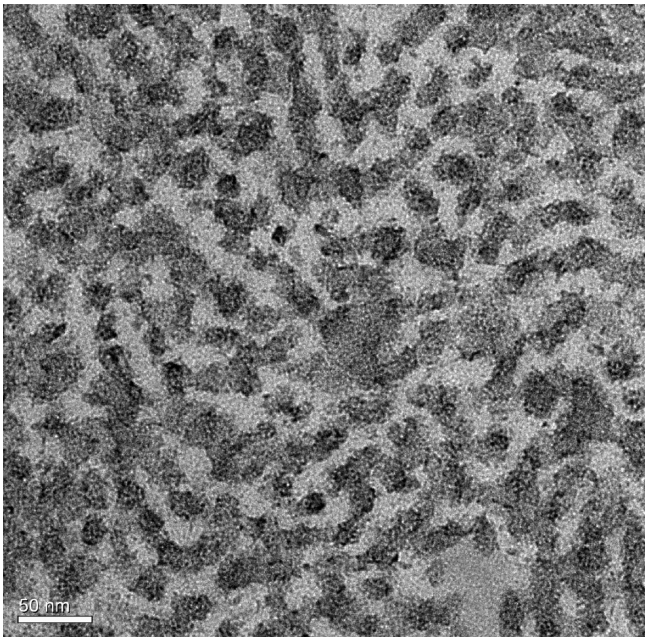

Figure 2. TEM image of the miktoarm star exposed to OsO_4 vapor for 24 h at room temperature followed by ultramicrotomy of the stained block to 60 nm sections. The analysis revealed dark cylinders (PI) surrounded by a PI/PS region, followed by a continuous (bright) PBLG phase.

consisted of two electrodes 20 mm in diameter and the sample with a thickness of about 50 μm (due to the high rigidity of the copolymers Teflon spacers were not necessary; the sample thickness was measured before and after the experiment and found to be unchanged). The complex dielectric permittivity $\varepsilon^* = \varepsilon' - i\varepsilon''$, where ε' is the real and ε'' is the imaginary part, is generally a function of frequency ω, temperature T, and pressure P, although here only the frequency and temperature dependencies have been investigated.[24] There are two principal mechanisms that contribute to ε^* in our case: orientation polarization of permanent dipoles (ε^*_{dip}) and conductivity contribution (ε^*_{cond}) as

$$\varepsilon^*(\omega, T, P) = \varepsilon^*_{dip}(\omega, T, P) - i\frac{\sigma(T, P)}{\varepsilon_f \omega} \quad (1)$$

where σ is the dc conductivity and ε_f is the permittivity of free space (=8.854 pF/m). The orientational contribution was fitted using the empirical equation of Havriliak and Negami[25]

$$\varepsilon^*_{dip}(\omega, T, P) = \varepsilon_\infty(T, P) + \sum_{k=1}^{2} \frac{\Delta\varepsilon_k(T, P)}{[1 + (i\omega\tau_{HN}(T, P)^{m_k}]^{n_k}} \quad (2)$$

where $\Delta\varepsilon_k(T,P)$ is the relaxation strength of the process under investigation, τ_{HN} is the relaxation time of the equation, m and n ($0 < m, mn \leq 1$) describe the symmetrical and asymmetrical broadening of the distribution of relaxation times, and $\varepsilon_\infty(T,P)$ is the dielectric permittivity at the limit of high frequencies. The relaxation times at maximum loss (τ_{max}) are presented herein and have been analytically obtained by the Havriliak−Negami equation as follows

$$\left[\sin\left(\frac{\pi m}{2+2n}\right)\right]^{1/m} \tau_{max} = \tau_{HN}\left[\sin\left(\frac{\pi mn}{2+2n}\right)\right]^{1/m} \quad (3)$$

At lower frequencies, ε'' rises due to the conductivity ($\varepsilon'' = \sigma/(\omega\varepsilon_f)$). The measured ε'' spectra have been used for the analysis except at high temperatures where the derivative of ε' has been employed ($d\varepsilon'/d \ln \omega \sim -(2/\pi)\varepsilon''$). Because ε' is not affected by the conductivity, this method is useful in fitting relaxation processes that are hidden under the conductivity, provided that the system is free of surface polarization effects. Therefore, the latter representation was employed in the analysis of the slower process (see Figure 5, below).

III. Results and Discussion

Local and Supramolecular Structure. Peptide local organization is determined by the dihedral angles (Φ and Ψ), which the individual amino-acid residues adopt in relation with the type of hydrogen bonding (intra- or intermolecular) they experience. This leads to two predominant types of polypeptide local conformations, α-helix and β-sheet, respectively, which can be differentiated by the ^{13}C chemical shifts of the peptide backbone C_α and C=O carbons, as well as the side chain C_α carbons. Thus, ^{13}C cross-polarization (CP) NMR spectroscopy performed at magic angle spinning (MAS) conditions has been extensively applied[26,27] and has nowadays established itself as the method of choice to gain doubtless information about the peptide secondary structures.[4,7,9,10,14,15,28,29]

The ^{13}C CP solid state NMR spectra of the PBLG-PS-PI star, shown in Figure 3, depicts peaks at about 176 and 56 ppm corresponding to the amide C=O and the C_α carbons of the PBLG backbone. These chemical shifts indicate the presence of α-helical conformations that are known to be stabilized in PBLG with more than 18 monomer units. Moreover, the absence of signals in the 52 ppm region, where

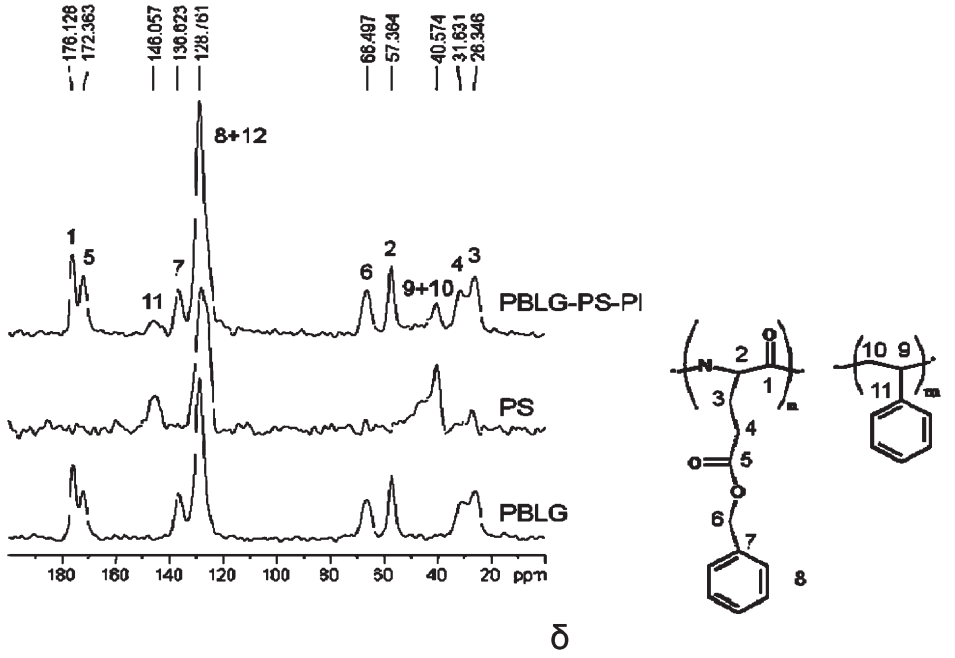

Figure 3. ^{13}C NMR profiles of $PBLG_{67}$ homopolypeptide, a PS homopolymer, and the miktoarm star. For $PBLG_{67}$, the intense peaks at $\delta \approx 176$ and 57.5 ppm arise from the amide C═O and C_α carbon, respectively, and indicate the formation of α-helical secondary structure. In the mitkoarm star, two C_α resonances are present, at 57.5 and 176 ppm, revealing that the PBLG blocks forms solely α-helical structures.

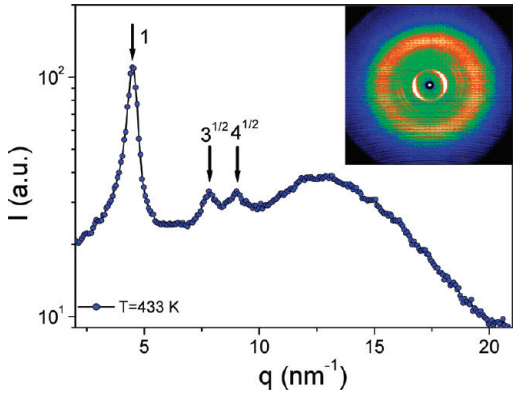

Figure 4. Equatorial WAXS intensity distribution of the miktoatm star plotted as a function of the scattering wave vector at 433 K. The arrows indicate the primary and higher order reflections from the hexagonal unit cell of PBLG. The 2D image obtained from an oriented fiber is also shown at the same temperature.

the C_α carbon associated with the β-sheet secondary structure resonate, shows the absence of these conformations in the polypeptide arm. The appearance of α-helical PBLG conformations in the star may suggest nanophase separation of the PBLG blocks in the star. This notion is supported by the WAXS investigation (Figure 4) from an oriented fiber that shows a sequence of equatorial reflections with relative positions at $1:3^{1/2}:4^{1/2}$ that correspond to the (10), (01), and (11) reflections of a hexagonal unit cell, with a lattice parameter $a = 1.59$ nm, reflecting the hexagonal packing of α-helices. These reflections, however, are broader and weaker when compared to bulk PBLG, indicating that the packing is hampered by the topological constraints at the star center. Nevertheless, NMR and WAXS clearly identified α-helical PBLG segments that are hexagonally packed, and this requires nanophase separated PBLG domains. This is in full accord with the conclusions from TEM, Figure 2, which suggest cylindrical PI domains within a continuous PBLG matrix.

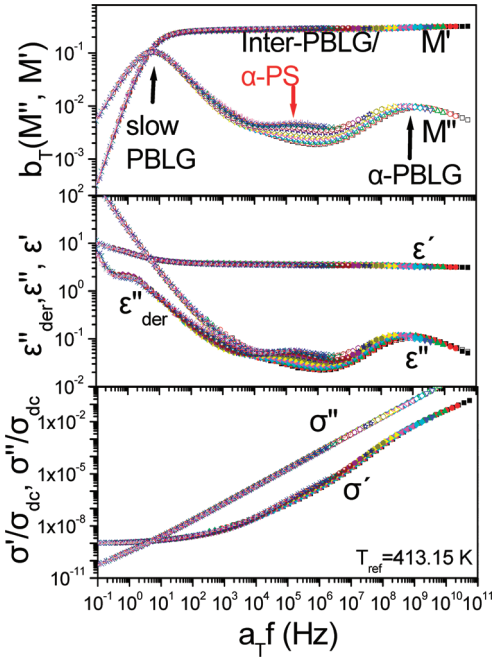

Figure 5. Superposition of the real and the imaginary parts of the electric modulus (top), M^*, of the complex dielectric permittivity (middle), ε^*, and of the conductivity σ^* for the miktoarm star at a reference temperature of 413.15 K. The data are in the range 321−453 K. The segmental (α-), intermediate, and "slow" processes of PBLG are indicated by arrows (see text).

With respect to the NMR spectra, notice that the methylene group of the PS backbone resonates at 41 ppm and the methyne moiety appears as a broad shoulder at slightly higher frequencies in the ^{13}C NMR spectrum. Both signals are inhomogeneously broadened, most probably due to the different stereochemistry of the PS backbone. Similar peak widths are observed in the PS homopolymer spectra (see Supporting Information), which in addition to the motional

behavior of the PS backbone and lower PS amount in the star, are the reasons for the lower signal intensity. Peak overlap and very low cross-polarization efficiency (in this temperature range the PI homopolymer is liquid-like, which leads to averaging of the dipole−dipole couplings) largely prohibit detecting the polyisoprene ^{13}C signals in the CP MAS NMR spectra.

Local Segmental Dynamics—Local Mixing. More decisive information on the details of nanophase separation can be obtained by experiments that can probe the local segmental dynamics of PI, PBLG, and PS in the star. For this purpose we employ dielectric spectroscopy and follow the local segmental dynamics of the different arms in comparison to the respective homopolymers.

The dielectric spectra of the star are depicted in Figure 5 as a function of reduced frequency for several temperatures in the range from 321.15 to 453.15 K relative to the reference temperature (413.15 K). The figure displays the real and imaginary parts of the electric modulus, the dielectric permittivity, and the conductivity that emphasize in a different way the dynamic processes. For example, whereas the electric modulus and the dielectric permittivity representations emphasize the dynamic processes associated with the PBLG, PS, and ion motions, the conductivity representation emphasizes the transition from the ac conductivity at higher frequencies to the dc conductivity at lower frequencies. Notice that in all representations the real and imaginary parts cross at a frequency that is characteristic of the ionic motion. Four processes are contributing within the temperature range shown in Figure 5. Starting from higher frequencies, these are[4] (i) the PBLG segmental process (α-process) associated with the relaxation of disordered chain segments created at defected hydrogen bonds and at the chain ends, (ii) an intermediate process reflecting both the contribution of the PS segmental relaxation and of the chain dynamics of disordered PBLG segments (see below), (iii) a slow process associated with the relaxation of the α-helical secondary structure that carries most of the dielectric signal, and (iv) the ion motion. These processes are known from bulk PBLG studies as a function of molecular weight, however, the second process in the star, indicated as intermediate PBLG/α-PS, has a higher intensity and a different shift factor than the weak intermediate process of PBLG. At even lower temperatures (not included in Figure 5), the segmental process of PI contributes to the dielectric response. The corresponding normal modes[30] of PI could not be detected as a separate process because of the overlapping frequencies with the PBLG α-process that is much stronger ($T\Delta\varepsilon$(α-PI) ∼ 25 K, $T\Delta\varepsilon$(α-PBLG) ∼ 300 K).

In Figure 6, the relaxation times for the four processes (PI segmental, PBLG segmental, mixed PS and PBLG intermediate process, and PBLG α-helical relaxation) were extracted and plotted in the usual Arrhenius representation. In the same figure, the homopolymer dynamics are depicted with lines, for example, the segmental and longest normal mode PI dynamics are shown with dashed and dash-dotted lines from a homopolymer with molecular weight of 11000 g/mol, the PBLG α-process with a black solid line (M_w = 10840 g/mol), the PBLG intermediate process with a dotted line, and the PS segmental relaxation with the red solid line. All four processes conform to the Vogel−Fulcher−Tammann (VFT) equation:

$$\tau = \tau_0 \exp\left(\frac{DT_0}{T - T_0}\right) \quad (4)$$

where τ_0 is the relaxation time in the high temperature limit, T_0 is the "ideal" glass temperature, and D is a dimensionless parameter. These parameters for the four processes in the star as well as for the corresponding homopolymers are summarized in Tables 2 and 3.

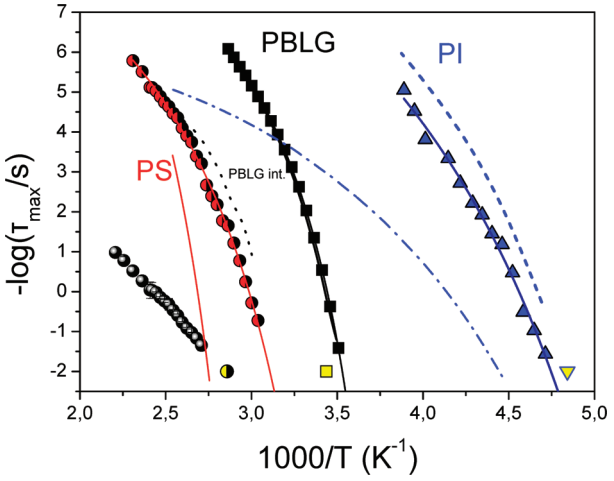

Figure 6. Arrhenius relaxation map of the dynamic processes in the miktoarm star obtained from dielectric spectroscopy. The segmental dynamics of PI in the star as shown by triangles. The dashed line represents the segmental dynamics of a PI homopolymer with similar molecular weight as the PI in the miktoarm ($M_w = 1.1 \times 10^4$ g/mol). The corresponding longest normal mode is shown by the dash-dotted line. The PBLG segmental dynamics in the star is shown by squares, whereas a black solid line indicates the corresponding segmental dynamics of a PBLG homopolymer. The intermediate mode of PBLG is plotted by the black dotted line. The segmental mode from a PS homopolymer ($M_w = 10^4$ g/mol) is plotted with a red line. The filled circles indicate a mixed PS segmental/PBLG intermediate process in the miktoarm star. The filled black circles correspond to the slow process associated with the PBLG broken helices. Lines are fits to the VFT equation. The DSC glass temperatures corresponding to the PI (triangle), PBLG (square), and PS (circle) blocks are shown at $\tau \sim 100$ s.

Table 2. VFT Parameters for the Different Processes in the Homopolymers

process	τ_0 (s)	D_T	T_0 (K)
α-PI	$(2.0 \pm 0.5) \times 10^{-13}$	8.8 ± 0.3	164.6 ± 0.9
normal mode -PI	$(1.5 \pm 0.5) \times 10^{-8}$	9.0 ± 0.1	160.8 ± 0.5
α- PS	$(5.0 \pm 0.5) \times 10^{-16}$	9.1 ± 0.5	296 ± 2
α- PBLG	$(5.0 \pm 0.5) \times 10^{-12}$	5.5 ± 0.2	241 ± 1
intermediate-PBLG	$(1.2 \pm 0.5) \times 10^{-8}$	3.1 ± 0.4	279 ± 5
slow-PBLG	$(2.5 \pm 0.5) \times 10^{-7}$	11 ± 4	206 ± 20

Table 3. VFT Parameters for the Different Processes in the (PS)(PI)(PBLG) Miktoarm Star

process	τ_0 (s)	D_T	T_0 (K)
α- PI	$(3.2 \pm 0.5) \times 10^{-12}$	8.8 ± 0.3	164.8 ± 0.7
α- PBLG	$(1.5 \pm 0.5) \times 10^{-11}$	4.7 ± 0.1	244 ± 1
α-PS/intermediate-PBLG	$(2.0 \pm 0.5) \times 10^{-11}$	8.2 ± 0.9	252 ± 5
slow-PBLG	$(7.2 \pm 0.5) \times 10^{-6}$	11 ± 4	213 ± 10

From an inspection of Figure 6, it becomes apparent that although the local segmental dynamics of PBLG are unaltered in the star with respect to the homopolymer, this is not the case with the PI and PS segmental dynamics. The PI segmental dynamics in the star are slowed down by about one decade, whereas the mixed PS/intermediate PBLG process is faster than the PS segmental dynamics in the homopolymer. This constitutes a clear proof of local mixing between the PI and PS segments, whereas the PBLG chains are well phase separated from the rest. This dynamic result is in excellent agreement with the structural investigation (NMR, WAXS) that revealed PBLG helical secondary structures organized in a hexagonal PBLG lattice

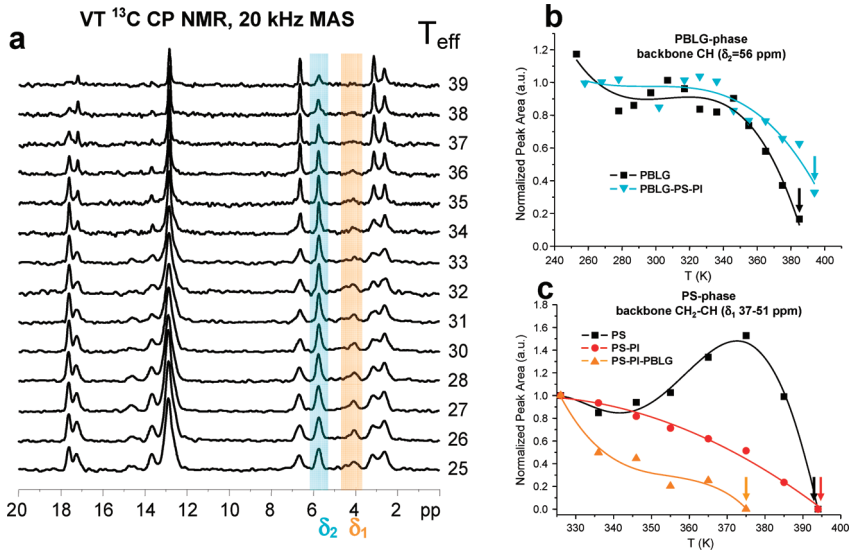

Figure 7. (a) Variable temperature (VT) ^{13}C cross-polarization (CP) NMR spectra of the PBLG-PI-PS star, recorded at 20 kHz magic angle spinning (MAS), with the PBLG backbone CH resonance at 56 ppm and the PS backbone CH_2−CH region (37−51 ppm) displayed in color. (b) Peak area of the PBLG backbone CH carbon resonance at 56 ppm presented as a function of temperature. The area is normalized to the lowest temperature signal at the diagram. Note the similar dynamic behavior of the PBLG backbone for the homopolymer and the star, which suggests PBLG phase separation in the star. (c) Peak area of the PS backbone CH_2−CH region at 37−51 ppm region in the ^{13}C NMR spectra presented as a function of temperature. The area is normalized to the lowest temperature signal at the diagram. The ~20 K difference in the temperatures at which the ^{13}C signal completely loses intensity indicates mixing between the PS and the PI phases.

as well as with the TEM results revealing a continuous PBLG phase.

To obtain further insight into the purity of phases at the local scale we have investigated the star and the respective PBLG (M_w = 14000 g/mol) and PS (M_w = 8400 g/mol) homopolymers as well as a microphase separated PS-*b*-PI diblock copolymer (M_w = 36040 g/mol, w_{PS} = 0.34) by variable temperature ^{13}C CP MAS NMR. In this experiment we take advantage of the signal loss that takes place when the frequency of the respective motion is matched by any of the following frequencies: (i) the frequency of the ^{1}H−^{13}C dipole−dipole couplings, (ii) the frequency of the decoupling field, or (iii) the frequency of the magic angle spinning (all in the range of 20 kHz). Figure 7a depicts the ^{13}C CP solid state NMR spectra of the star at several temperatures whereas the respective spectra for the homopolymer PBLG (Figure S1), the PS homopolymer (Figure S2) and the diblock PS-PI (Figure S3) are provided in the Supporting Information. In Figure 7a, the resonances at 56 ppm and within the range 37−51 ppm, that correspond to the PBLG backbone CH group and the PS backbone CH_2−CH moieties, are marked by different colors. The area of these resonances, normalized to the respective area at the lowest temperature investigated, is displayed as a function of temperature in Figure 7b,c. The general trend is for a decreasing peak area on heating due to enhancing the system mobility. This results in the reduction of the effective dipole−dipole couplings and respectively lower cross-polarization efficiency at higher temperatures. For bulk PBLG as well as for the PBLG in the miktoarm star, this intensity reduction is apparent at elevated temperatures in the C_α (ca. 56 ppm) region as well as in the C=O (ca. 176 ppm) region. There is only a slight shift of 5−10 K of the PBLG dynamics in the star to higher temperatures (Figure 7b). Nevertheless, this confirms the similarity in the dynamics of PBLG in the star with the respective homopolymer. In addition, the C_α methylene group at 27 ppm, which is directly attached to the backbone, also suffers signal loss on heating, but to a lesser degree than the backbone.

The temperature dependence of the normalized peak area for the PS backbone CH_2−CH in the star, as well as the PS-*b*-PI block copolymer and the homopolymer, is plotted in Figure 7c. In the case of the PS homopolymer (Figure S2), the ^{13}C resonances of the backbone and the phenyl ring lose intensity in the ^{13}C CP MAS NMR spectra at the same temperature (ca. 395 K). Thus, a uniform dynamic of the PS backbone and side group is observed at the NMR frequency. Notice that the signal intensity corresponding to the PS backbone in the homopolymer as well as in the PS-*b*-PI is reduced to zero at the same temperature (ca. 395 K). This suggests nanophase separation between the PS and the PI blocks in the copolymer, which is confirmed by SAXS (cylindrical nanodomain with an intercylinder distance of 38.2 nm). However, in the case of the star, the respective intensity reduces to zero at about 375 K, that is, some 20 K lower than in the PS homopolymer and nanophase separated diblock copolymer. This is in excellent agreement with the acceleration of the PS segmental dynamics found in DS. Thus, both ^{13}C NMR and DS revealed intact PBLG local dynamics as opposed to the accelerated PS dynamics that further suggest a pure PBLG phase and mixed PS and PI phases in the star.

Dynamics of the α-Helical PBLG Structure. The dynamics of the secondary structure (α-helix) can be obtained from DS from the slower and more intense process associated, in principle, with the end-to-end relaxation of dipoles in a perfect α-helical structure. DS is very sensitive not only to the presence of α-helices but also to their persistence length. In this respect, we have recently shown[4] that, contrary to the expectation born out by the static experiments and common belief, α-helical polypeptides cannot be considered as ideal rigid rods and that a model of "broken" rods is closer to reality. This is based on the fact that there exist two processes above the T_g that are slower than the segmental (α-) process: an "intermediate" process that has strong molecular weight dependence and reflects the relaxation of amorphous parts of PBLG chains and a "slow" process that reflects the relaxation of α-helical defects. The persistence length, ξ, of the α-helical structure can be extracted from the intensity of the slower DS process. In a study of PBLG as a function of molecular weight, ξ was found in the range of 1−2 nm, that is, comprising about 10−20 monomers.[4]

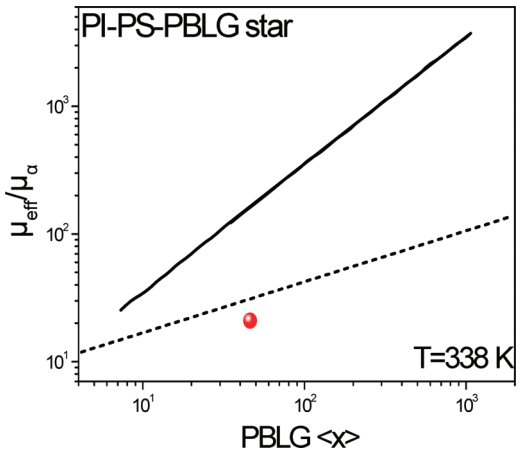

Figure 8. Normalized effective dipole moment of the miktoarm star (●), calculated from the intensity of the slower process and divided by the dipole moment of the corresponding α-process. The continuous line is the theoretical dipole moment for an ideal α-helix (3.4 debye per monomer), and the dashed line is the calculated effective dipole moment for bulk PBLG. Notice that all experimental data points, both for PBLG homopolymers and for PBLG in the star, are lying below the theoretical value, implying that the helices are broken in several pieces.

In view of these recent results, it is of interest to explore the effect of the 3-miktoarm star topology on the persistence length of the PBLG α-helical structure. To make the comparison more quantitative, we plot in Figure 8 the dipole moment corresponding to the "slow" process normalized to its value for the α-process and compare it to the bulk PBLG case. The dipole moment was calculated using the Buckingham equation,[31] applicable to rod-like molecules in solution

$$\frac{Nfg\mu^2}{3\varepsilon_0 k_B T} = \frac{(2\varepsilon_s+1)(\varepsilon_s-n^2)}{2\varepsilon_s+n^2} - \frac{(2\varepsilon_\infty+1)(\varepsilon_\infty-n^2)}{2\varepsilon_\infty+n^2} \quad (5)$$

where μ is the dipole moment, N is the number density of dipoles, $g = 1 + \langle\cos\gamma\rangle$ is the Kirkwood−Fröhlich correlation factor between neighboring dipoles, ε_s and ε_∞ are the permittivity values at the low and high frequency limit, respectively, f is a value related to the geometry of the molecule ($f \rightarrow {}^2/_3$ for an infinitely long rod), and n is the refractive index. The solid line in Figure 8 gives the theoretical dipole moment for a perfect α-helix ($\mu_{eff} \sim x \cdot 3.4$ debye). The dashed line shows the respective values for a series of PBLG homopolymers. As it can be seen, the effective dipole moment of PBLG in the miktoarm star corresponds to that of a defected helix.

Recently,[32,33] a simple model of "defected" helices has been proposed to account for these results in bulk PBLG. Briefly, the helix is assumed to be composed of N_P "ideal" helical parts of equal length ξ (the persistence length) that can rotate on the surface of a cone of angle θ. The rotation of each part is assumed to be independent from the others, but the axes of all cones are parallel. This is a reasonable assumption, because X-ray measurements from oriented fibers both in bulk PBLG as well as in the star (Figure 4) have shown that helices are hexagonally packed. The dipole moment of each part is $\mu_P = 3.4$ debye$\cdot(\xi/0.15$ nm), given that the α-helix length is 0.15 nm/monomer. The total dipole moment is calculated as[32,33]

$$\Delta\varepsilon = \frac{N_A\rho}{3\varepsilon_0 kTM_m}(3.4 \text{ debye})^2(\xi/0.15 \text{ nm})\sin^2\theta \quad (6)$$

and the only parameter that is needed in calculating ξ is the angle θ. In the X-ray scattering patterns from oriented fibers

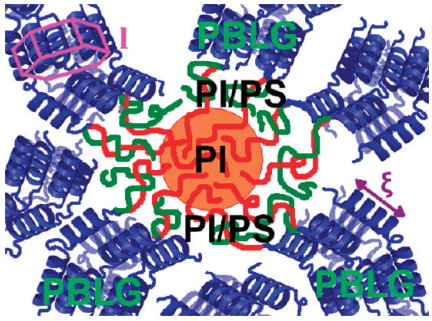

Figure 9. Schematic representation of the miktoarm star structure showing PBLG domains (blue) composed from α-helices that are hexagonally packed with a persistence length, ξ, that is lower than in bulk PBLG. In the center, PI cylinders (red) are shown that are separated from the PBLG domains with a mixed PI/PS region.

of bulk PBLG an upper limit in the angle was obtained as $\theta_{max} \sim 0.25$ rad. This angle results in a minimum value for $\xi \sim 2$ nm for bulk PBLG and to a somewhat smaller value for the PBLG arm in the star. Thus, despite the α-helical secondary structure (NMR, WAXS) and the hexagonal packing of α-helices (WAXS), the PBLG helices in the star are far from being ideal and contain many structural defects. The effect of star topology is to increase the number of defected hydrogen bonds that effectively reduce the persistence length of α-helices.

The structure and dynamics investigation results in the "dynamic" self-assembly depicted in a schematic but realistic way in Figure 9. The schematic depicts pure PBLG domains (based on the results of dielectric spectroscopy, NMR and TEM), an intermediate phase composed of mixed segments of PS/PI (from dielectric spectroscopy, NMR and TEM) and an inner part composed from PI cylindrical domains (TEM). NMR revealed that PBLG forms α-helices that are further assembled in a hexagonal lattice of length l (from X-rays), despite being broken at several places (i.e., with a reduced helix persistence length, ξ) as compared to the bulk.

IV. Conclusions

The investigation of the self-assembly in the (PS)(PI)(PBLG) miktoarm star chimera revealed that the peptidic block possesses the same level of hierarchy as the homopolypeptide, that is, α-helices stabilized by intramolecular hydrogen bonds (NMR, WAXS), that are further assembled into a hexagonal lattice (WAXS). The investigation of the dynamics by employing local probes of phase mixing (DS and NMR) further elucidated the self-assembly. The peptidic block is nanophase separated into pure PBLG domains, whereas the amorphous blocks are partially mixed (DS, NMR, TEM). Furthermore, the effect of the star topology is to increase the number of defected hydrogen bonds within the PBLG arms and to reduce the persistence length of the α-helical structures (DS).

This level of structural detail is nowadays possible by combining structural information at the nanometer (NMR, WAXS) and submicrometer (TEM) length scales with independent dynamic information at the segmental (DSC, NMR, DS) and α-helical (DS) length scales.

Acknowledgment. This work was cofinanced by the E.U.-European Social Fund (75%) and the Greek Ministry of Development, GSRT (25%), in the framework of the program PENED2003 (No. 856). We thank A. Best, M. Bach (MPI-P), and G. Tsoumanis (UoI) for technical support. Financial support of the Deutsche Forschungsgemeinschaft, SFB 625, is gratefully acknowledged.

Supporting Information Available: VT ^{13}C CP NMR spectra of PBLG, PS, and PS-PI. This material is available free of charge via the Internet at http://pubs.acs.org.

References and Notes

(1) Hadjichristidis, N.; Pispas, S.; Floudas, G. *Block Copolymers: Synthetic Strategies, Physical Properties and Applications*; J. Wiley and Sons: NJ, 2003.
(2) Hamley, I. W. *The Physics of Block Copolymers*; Oxford University Press: Oxford, 1998.
(3) Bates, F. S.; Fredrickson, G. H. *Annu. Rev. Phys. Chem.* **1990**, *41*, 525.
(4) Papadopoulos, P.; Floudas, G.; Klok, H.-A.; Schnell, I.; Pakula, T. *Biomacromolecules* **2004**, *5*, 81.
(5) Sary, N.; Rubatat, L.; Brochon, C.; Hadziioannou, G.; Ruokolainen, J.; Mezzenga, R. *Macromolecules* **2007**, *40*, 6990.
(6) Klok, H.-A.; Lecommandoux, S. *Adv. Polym. Sci.* **2006**, *202*, 75.
(7) Floudas, G.; Papadopoulos, P.; Klok, H.-A.; Vandermeulen, G. W. M.; Rodriguez-Hernandez, J. *Macromolecules* **2003**, *36*, 3673.
(8) Reenders, M.; ten Brinke, G. *Macromolecules* **2002**, *35*, 3266.
(9) Papadopoulos, P.; Floudas, G.; Schnell, I.; Lieberwirth, I.; Nguyen, T. Q.; Klok, H.-A. *Biomacromolecules* **2006**, *7*, 618.
(10) Papadopoulos, P.; Floudas, G.; Schnell, I.; Aliferis, T.; Iatrou, H.; Hadjichristidis, N. *Biomacromolecules* **2005**, *6*, 2352.
(11) Floudas, G.; Hadjichristidis, N.; Iatrou, H.; Pakula, T.; Fischer, E. W. *Macromolecules* **1994**, *27*, 7735.
(12) Floudas, G.; Pispas, S.; Hadjichristidis, N.; Pakula, T.; Erukhimovich, I. *Macromolecules* **1996**, *29*, 4142.
(13) Duran, H.; Gitsas, A.; Floudas, G.; Mondeshki, M.; Steinhart, M.; Knoll, W. *Macromolecules* **2009**, *42*, 2881.
(14) Gitsas, A.; Floudas, G.; Mondeshki, M.; Butt, H.-J.; Spiess, H. W.; Iatrou, H.; Hadjichristidis, N. *Biomacromolecules* **2008**, *9*, 1959.
(15) Gitsas, A.; Floudas, G.; Dietz, M.; Mondeshki, M.; Spiess, H. W.; Wegner, G. *Macromolecules* **2007**, *40*, 8311.
(16) Minich, E. A.; Nowak, A. P.; Deming, T. J.; Pochan, D. J. *Polymer* **2004**, *45*, 1951.
(17) Abraham, S.; Ha, C.-S.; Kim, I. *J. Polym. Sci., Part A: Polym. Chem.* **2006**, *44*, 2774.
(18) Babin, J.; Taton, D.; Brinkmann, M.; Lecommandoux, S. *Macromolecules* **2008**, *41*, 1384.
(19) Karatzas, A.; Iatrou, H.; Hadjichristidis, N.; Inoue, K.; Sugiyama, K.; Hirao, A. *Biomacromolecules* **2008**, *9*, 2072.
(20) Langer, B.; Schnell, I.; Spiess, H. W.; Grimmer, A.-R. *J. Magn. Reson.* **1999**, *138*, 182.
(21) Metz, G.; Wu, X.; Smith, S. O. *J. Magn. Reson.* **1994**, *110*, 219.
(22) Bennett, A. E.; Rienstra, C. M.; Auger, M.; Lakshmi, K. V.; Griffin, R. G. *J. Chem. Phys.* **1995**, *103*, 6951.
(23) Fischbach, I.; Pakula, T.; Minkin, P.; Fechtenkötter, A.; Müllen, K.; Spiess, H. W.; Saalwächter, K. *J. Phys. Chem. B* **2002**, *106*, 6408.
(24) Floudas, G. In *Broadband Dielectric Spectroscopy*; Kremer, F., Schönhals, A., Eds.; Springer: Berlin, 2002, Chapter 8.
(25) Havriliak, S.; Negami, S. *Polymer* **1967**, *8*, 161.
(26) Kricheldorf, H. R.; Müller, D. *Macromolecules* **1983**, *16*, 615.
(27) Saito, H.; Tabeta, R.; Shoji, A.; Ozaki, T.; Ando, I. *Macromolecules* **1983**, *16*, 1050.
(28) Koynov, K.; Mihov, G.; Mondeshki, M.; Moon, C.; Spiess, H. W.; Müllen, K.; Butt, H.-J.; Floudas, G. *Biomacromolecules* **2007**, *8*, 1745.
(29) Mondeshki, M.; Mihov, G.; Graf, R.; Spiess, H. W.; Müllen, K.; Papadopoulos, P.; Gitsas, A.; Floudas, G. *Macromolecules* **2006**, *39*, 9605.
(30) Stockmayer, W. H. *Pure Appl. Chem.* **1967**, *15*, 539. Floudas, G. T.; Reisinger, T. *J. Chem. Phys.* **1999**, *111*, 5201.
(31) Buckingham, A. D. *Aust. J. Chem.* **1953**, *6*, 323.
(32) Papadopoulos, P.; Floudas, G. *Dielectrics Newsletter*; Nov. 2005.
(33) Floudas, G.; Spiess, H. W. *Macromol. Rapid Commun.* **2009**, *30*, 278.